Auxiliary Material

Revisiting the North Chile seismic gap segmentation using GPS-derived interseismic coupling

1 Detail of GPS data set

1.1 New data set

For the purpose of this study, we reprocessed several campaign measurements conducted between 2000 and 2008 and combined those with recent measurements conducted in 2010, 2011 and 2012. The regional network obtained is presented in figure 1 and includes several permanent stations of Caltech and GFZ (IPOC). Each point of the network has its own measurement history (see supp. Table 2) and the interseismic velocities are obtained over varying time spans. For instance, the southernmost Paranal profile has been measured six times in an eleven years time-span (2000-2011), and because no major earthquake occurred there since 2000, the velocity at those points is purely interseismic and very well constrained. On the contrary, the interseismic velocity on the new benchmarks installed in 2010 (Pisagua or Pica profiles in supp. Table 2 and Fig. 2 in the main text) are based on only two measurements over a two years time span (2010-2012). The Tocopilla and Mejillones areas were affected by the 2007 Mw 7.7 Tocopilla earthquake. Therefore, we use only measurements acquired after 2008. No clear postseismic motion associated with this event is registered in the campaign time-series (see linear trend at TO30 in supp. Fig. 4). Similarly, the 2005 Tarapaca earthquake produced coseismic deformation all along the Iquique profile, which leads us to exclude pre-Tarapaca measurements on this profile to get the interseismic velocity. On most of the points, the velocity is constrained by three measurements over a seven years time span.

All together, data from 83 regional permanent stations and campaign benchmarks were processed together with 28 continuous stations located on either the South-America craton or the Nazca plate. The baselines repeatabilities associated with each campaign (see supp. Table 1) indicate that the horizontal components of the relative position vectors are precise to within 3 millimeters (the most recent the best) whereas vertical component precision varies between 3 and 9 mm through time. We combined the daily solutions using GLOBK and we present in supp. Table 2 and Table 3 the interseismic velocities both in the ITRF2008 and in the fixed NNR-Nuvel1A South America. We plot in supplementary Figure 3 the stations used in the stabilization procedure and some of the Brazilian and Argentine permanent stations that constrain the South America craton.

Campaign	2000	2005	2007	2008	2008-2	2010	2011	2012
North	1.2	1.0	1.2	0.6	1.0	0.7	0.8	1.4
East	3.5	0.6	1.6	0.9	1.2	0.8	1.0	1.8
Vert	9.1	3.2	3.8	2.8	4.3	3.9	2.8	5.3

Table 1: Repeatability (σ of distribution) for each campaign on North, East and vertical components.

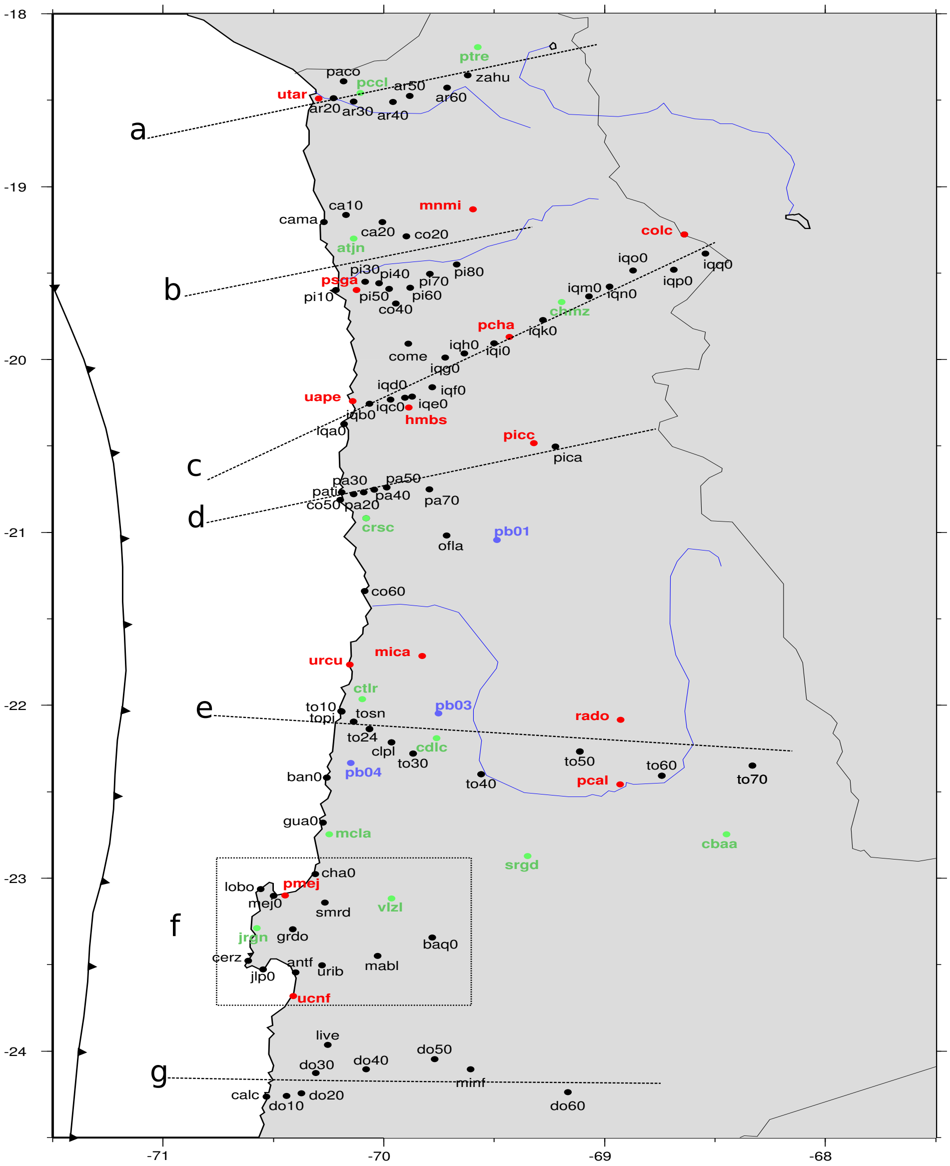

Figure 1: International network of c-GPS and s-GPS stations used in our processing. Black dots : Franco-Chilean campaign benchmarks. Red dots : Franco-Chilean permanent stations. Blue dots : GFZ German permanent stations. Green dots : Caltech permanent stations.

YEAR	00	05	07	08	08-2	10	11	12
a- Profile Arica								
AR20	-	-	-	-	-	X	-	X
PACO	-	X	-	-	-	X	-	X
AR30	-	-	-	-	-	X	-	X
AR40	-	-	-	-	-	X	-	X
AR50	-	-	-	-	-	X	-	X
AR60	-	-	-	-	-	X	-	X
ZAHU	-	X	-	-	-	X	-	X
b- Profile Pisagua								
CAMA	-	-	-	-	-	X	-	X
CA10	-	-	-	-	-	X	-	X
CA20	-	-	-	-	-	X	-	X
CO20	-	-	-	-	-	X	-	X
CO40	-	X	-	-	-	X	-	X
PI10	-	-	-	-	-	X	-	X
PI30	-	-	-	-	-	X	-	X
PI40	-	-	-	-	-	X	-	X
PI50	-	-	-	-	-	X	-	X
PI60	-	-	-	-	-	X	-	X
PI70	-	-	-	-	-	X	-	X
PI80	-	-	-	-	-	X	-	X
c- Profile Iquique								
COME	-	-	-	-	-	X	-	X
IQA0	-	X	-	-	-	X	-	X
IQB0	-	-	-	-	-	X	-	X
IQC0	-	-	-	-	-	X	-	X
IQD0	-	X	-	-	-	-	-	X
IQE0	-	-	-	-	-	X	-	X
IQF0	-	X	-	-	-	X	-	X
IQG0	-	X	-	-	-	X	-	X
IQH0	-	X	-	-	-	X	-	X
IQI0	-	X	-	-	-	X	-	X
IQK0	-	X	-	-	-	X	-	X
IQM0	-	X	-	-	-	X	-	X
IQN0	-	-	-	-	-	X	-	X
IQO0	-	X	-	-	-	X	-	X
IQP0	-	X	-	-	-	X	-	X
IQQ0	-	X	-	-	-	X	-	X
d- Profile Pica								
CO50	-	-	-	X	X	X	-	X
CO60	-	-	-	X	X	-	-	X
OFLA	-	X	-	-	-	X	-	X
PA20	-	-	-	-	-	X	-	X
PA30	-	-	-	-	-	X	-	X
PA40	-	-	-	-	-	X	-	X
PA50	-	-	-	-	-	X	-	X
PA70	-	-	-	-	-	X	-	X
PATI	-	-	-	-	-	X	-	X
PICA	-	X	-	-	-	X	-	X

YEAR	00	05	07	08	08-2	10	11	12
e- Profile Tocopilla								
BANA	-	-	-	X	X	X	X	X
CLPL	-	-	-	-	-	X	X	X
TO1A	-	-	-	X	X	X	-	-
TO24	-	-	-	-	-	X	X	X
TO3A	-	-	-	X	X	X	X	X
TO40	-	-	-	-	-	X	X	X
TO5A	-	-	-	X	X	X	X	X
TO6A	-	-	-	-	X	X	X	X
TO7A	-	-	-	-	X	X	X	X
TOPI	-	-	-	-	-	X	X	X
TOSN	-	-	-	-	-	X	X	X
f- Mejillones area								
CHAA	-	-	-	X	X	X	X	X
GUA0	-	-	X	X	X	X	X	X
LOBO	-	-	-	-	-	X	X	X
MEJ0	-	-	-	X	-	X	X	X
SMRD	-	-	-	-	-	X	X	X
GRDO	-	-	-	-	-	X	X	X
CERZ	-	-	-	-	-	X	X	X
JLPA	-	-	-	X	X	X	X	X
ANTA	-	-	-	-	-	X	X	X
URIA	-	-	-	-	-	X	X	X
BAQA	-	-	-	-	X	X	X	X
MABL	-	-	-	-	-	X	X	X
g- Profile Paranal								
DO10	-	-	X	X	X	X	X	-
DO20	X	-	X	X	X	X	X	-
DO30	-	-	X	X	X	X	X	-
DO40	X	-	X	X	X	X	X	-
DO50	X	-	X	X	X	X	X	-
DO60	X	-	X	X	X	X	X	-
CALC	-	X	-	-	-	X	X	-
LIVE	-	-	-	-	-	X	X	-
MINF	-	-	-	-	-	X	X	-

Figure 2: Table of measurement for each campaign since 2000.

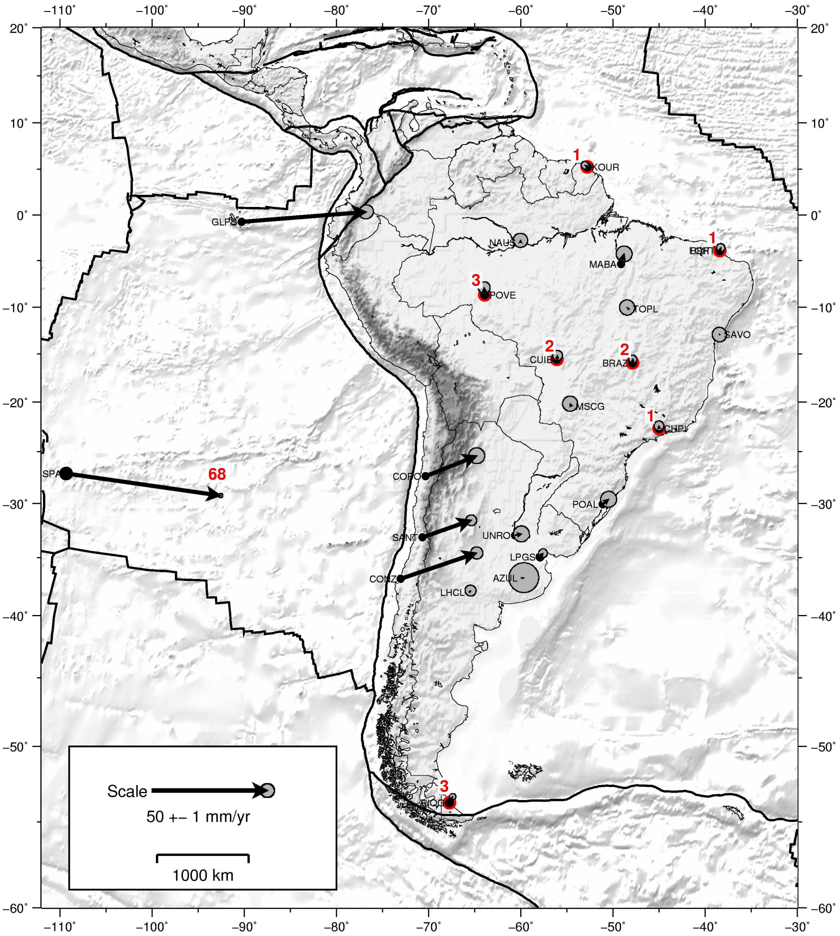

Figure 3: Large scale network and far field velocities. Dots show locations of cGPS stations. Arrows depict their horizontal velocities with respect to a reference frame fixed on the South-American craton constrained by the red-dot stations. Bold numbers aside the arrows indicate the velocity in mm/yr. Ellipses depict the region of 99% confidence.

SITE	Position		Velocity-ITRF08		Velocity-Nuvel1A		Uncertainties		r
	Lon.	Lat.	Vlon	Vlat	Vlon	Vlat	σ_{lon}	σ_{lat}	
ANTF	289.599	-23.544	30.91	19.57	33.14	10.61	1.54	1.54	-0.005
AR20	289.772	-18.489	13.43	15.76	16.36	6.78	1.63	1.60	-0.001
AR30	289.864	-18.508	14.41	15.56	17.35	6.57	1.61	1.58	0.000
AR40	290.042	-18.510	12.49	18.03	15.44	9.02	1.54	1.54	-0.002
AR50	290.117	-18.475	11.25	13.66	14.20	4.64	1.60	1.57	-0.004
AR60	290.287	-18.427	10.65	18.23	13.62	9.19	1.57	1.56	-0.003
BAN0	289.742	-22.417	28.21	20.34	30.60	11.36	1.15	1.15	-0.005
BAQU	290.219	-23.342	23.74	17.39	26.03	8.36	1.14	1.14	-0.006
CA10	289.828	-19.164	18.78	18.51	21.63	9.52	1.66	1.61	0.007
CA20	289.993	-19.206	16.95	15.20	19.80	6.19	1.61	1.58	0.004
CALC	289.468	-24.264	30.03	17.53	32.15	8.58	0.75	0.75	-0.006
CAMA	289.729	-19.206	17.65	17.50	20.48	8.52	1.60	1.57	-0.014
CERZ	289.386	-23.476	31.97	19.86	34.19	10.92	1.55	1.54	-0.004
CHA0	289.690	-22.976	22.60	18.15	24.91	9.18	1.08	1.09	-0.006
CLPL	290.035	-22.214	22.94	17.82	25.38	8.81	1.54	1.54	-0.003
CO20	290.103	-19.288	15.87	17.60	18.71	8.58	1.59	1.57	-0.001
CO40	290.054	-19.677	18.04	16.00	20.83	6.99	0.82	0.83	-0.002
CO50	289.802	-20.812	24.12	18.17	26.74	9.19	1.08	1.08	-0.004
CO60	289.913	-21.340	25.20	18.72	27.75	9.72	1.08	1.08	-0.005
COME	290.111	-19.908	16.88	14.45	19.64	5.43	1.55	1.53	-0.002
DO10	289.560	-24.260	28.98	18.69	31.11	9.73	1.13	1.13	-0.007
DO20	289.627	-24.244	28.72	17.76	30.85	8.80	0.68	0.68	-0.005
DO30	289.692	-24.127	29.09	17.45	31.24	8.48	1.14	1.14	-0.002
DO40	289.920	-24.105	26.06	16.86	28.23	7.86	0.68	0.68	-0.004
DO50	290.231	-24.045	24.34	16.42	26.54	7.39	0.68	0.69	-0.004
DO60	290.834	-24.236	18.18	17.09	20.39	7.99	0.68	0.68	-0.005
GRDO	289.588	-23.294	27.71	22.84	29.97	13.88	1.56	1.55	-0.004
GUA0	289.724	-22.679	22.78	16.71	25.14	7.73	1.02	1.02	-0.006
IQA0	289.820	-20.373	19.48	16.09	22.16	7.10	0.83	0.83	-0.003
IQB0	289.936	-20.256	18.67	14.71	21.37	5.71	1.55	1.54	-0.003
IQC0	290.031	-20.231	23.63	16.87	26.34	7.86	1.56	1.55	-0.003
IQD0	290.096	-20.221	17.63	15.07	20.35	6.05	0.83	0.83	-0.003
IQE0	290.128	-20.214	20.24	16.69	22.96	7.67	1.56	1.55	-0.003
IQF0	290.219	-20.160	17.75	15.30	20.48	6.27	0.83	0.83	-0.003
IQG0	290.277	-19.988	17.64	15.55	20.40	6.51	0.82	0.83	-0.003
IQH0	290.364	-19.964	17.04	16.55	19.81	7.50	0.82	0.83	-0.003
IQI0	290.499	-19.907	17.57	16.22	20.35	7.16	0.83	0.83	-0.003
IQK0	290.720	-19.771	17.75	16.98	20.56	7.89	0.82	0.83	-0.003
IQM0	290.930	-19.636	17.36	17.79	20.20	8.68	0.82	0.83	-0.002
IQN0	291.022	-19.579	15.50	19.17	18.35	10.05	1.54	1.53	-0.002
IQO0	291.129	-19.485	13.06	18.91	15.93	9.78	0.82	0.83	-0.002
IQP0	291.314	-19.481	14.76	19.17	17.64	10.02	0.82	0.82	-0.002
IQQ0	291.456	-19.387	13.55	17.56	16.45	8.39	0.82	0.83	-0.002
JLP0	289.454	-23.526	29.45	20.44	31.67	11.49	1.08	1.08	-0.007
LIVE	289.747	-23.964	29.31	18.82	31.49	9.84	2.11	2.10	-0.003
LOBO	289.443	-23.062	25.32	21.60	27.61	12.66	1.55	1.54	-0.004
MABL	289.972	-23.448	24.89	16.90	27.15	7.90	1.54	1.54	-0.004
MEJ0	289.501	-23.102	24.79	19.37	27.07	10.42	1.08	1.08	-0.006
MINF	290.394	-24.105	21.76	18.21	23.96	9.16	2.13	2.11	-0.003
OFLA	290.284	-21.018	21.62	15.18	24.24	6.14	0.84	0.85	-0.004
PA20	289.863	-20.778	21.87	20.43	24.50	11.44	1.55	1.55	-0.002
PA30	289.909	-20.768	22.43	19.93	25.06	10.93	1.55	1.54	-0.003
PA40	289.956	-20.753	20.84	19.47	23.48	10.47	1.55	1.54	-0.002
PA50	290.013	-20.740	21.65	17.06	24.29	8.05	1.54	1.53	-0.002
PA70	290.206	-20.750	17.24	19.53	19.89	10.50	1.62	1.59	0.008
PACO	289.817	-18.391	12.54	15.50	15.49	6.51	0.84	0.85	0.000
PATI	289.810	-20.768	20.40	19.19	23.03	10.20	1.55	1.55	-0.004
PI10	289.783	-19.598	19.12	15.34	21.90	6.36	1.58	1.56	-0.002
PI30	289.915	-19.551	19.51	17.56	22.31	8.56	1.62	1.60	0.000
PI40	289.978	-19.560	19.08	17.37	21.88	8.37	1.57	1.56	-0.006
PI50	290.023	-19.592	18.46	17.03	21.26	8.02	1.58	1.57	-0.003
PI60	290.120	-19.586	17.91	18.84	20.71	9.82	1.58	1.56	0.000
PI70	290.208	-19.505	18.16	16.02	20.98	6.99	1.59	1.56	-0.001
PI80	290.330	-19.451	16.19	17.14	19.02	8.10	1.62	1.59	-0.002
PICC	290.665	-20.490	17.63	16.97	20.34	7.89	1.52	1.52	-0.002
SMRD	289.733	-23.140	22.87	19.07	25.16	10.09	1.57	1.56	-0.002
TO10	289.808	-22.035	26.31	20.79	28.76	11.81	1.51	1.51	-0.005
TO24	289.935	-22.137	23.64	17.67	26.08	8.67	1.54	1.54	-0.003
TO30	290.133	-22.279	24.55	17.40	26.99	8.38	1.10	1.09	-0.006
TO40	290.440	-22.398	21.44	20.76	23.88	11.70	1.56	1.55	-0.003
TO50	290.889	-22.267	15.38	15.63	17.86	6.53	1.09	1.09	-0.005
TO60	291.259	-22.407	13.63	15.14	16.12	6.00	1.16	1.16	-0.006
TO70	291.670	-22.349	12.86	15.34	15.38	6.15	1.16	1.16	-0.006
TOPI	289.806	-22.034	28.10	18.94	30.55	9.96	1.57	1.56	-0.005
TOSN	289.864	-22.095	21.97	19.24	24.42	10.25	1.56	1.56	-0.001
URIB	289.720	-23.505	26.60	21.16	28.84	12.18	1.54	1.54	-0.004
ZAHU	290.380	-18.357	8.59	16.15	11.57	7.10	0.72	0.72	0.005

Table 2: Horizontal velocities in mm/yr on the campaign network. Vlat and Vlon are given in mm/yr either in the ITRF2008 reference frame (columns 3 and 4), or in the NNR-Nuvel1A South-America fixed reference frame (columns 5 and 6), 7 is the correlation between horizontal components.

SITE	Position		Velocity-ITRF08		Velocity-NNR		Uncertainties		r
	Lon.	Lat.	Vlon	Vlat	Vlon	Vlat	σ_{lon}	σ_{lat}	
ANTC^{i}	288.468	-37.339	15.70	10.12	15.84	1.29	0.87	0.86	-0.032
ATJN^{c}	289.863	-19.301	16.19	15.80	19.02	6.81	1.01	1.01	-0.002
AZUL^{a}	300.119	-36.767	-0.55	10.10	0.83	0.11	2.14	2.13	0.005
BATF^{b}	320.257	-17.555	-12.56	15.90	-7.86	4.90	1.56	1.58	-0.006
BRAZ^{i*}	312.122	-15.947	-4.22	12.38	0.13	1.63	0.58	0.58	-0.017
BRFT^{i*}	321.574	-3.877	-4.68	12.24	0.50	1.22	0.60	0.59	-0.048
CBAA^{c}	291.552	-22.746	10.99	16.28	13.45	7.10	1.21	1.22	-0.004
CDLC^{c}	290.238	-22.190	21.26	15.71	23.71	6.68	1.12	1.12	-0.004
CEEU^{b}	321.574	-3.878	-2.88	11.97	2.30	0.95	1.10	1.11	-0.041
CFAG^{i}	291.767	-31.602	6.02	11.38	7.28	2.18	0.71	0.71	-0.022
CHMZ^{c}	290.806	-19.669	16.49	17.91	19.32	8.81	1.30	1.31	-0.001
CHPI^{i*}	315.015	-22.687	-4.20	12.03	-0.13	1.16	0.69	0.70	0.001
COLC^{f}	291.361	-19.276	13.19	18.32	16.10	9.16	1.01	1.01	-0.002
CONZ^{g}	286.975	-36.844	32.91	19.85	32.99	11.19	0.87	0.87	-0.034
COPO^{i}	289.662	-27.385	20.57	17.80	22.26	8.83	1.14	1.14	-0.010
CRSC^{c}	289.920	-20.918	23.63	18.78	26.24	9.78	1.01	1.01	-0.004
CTLR^{p}	289.903	-21.964	25.06	19.32	27.53	10.32	1.12	1.12	-0.004
CUIB^{b*}	303.930	-15.555	-3.76	11.90	0.21	1.62	0.72	0.72	-0.001
GLPS^{i}	269.696	-0.743	49.01	10.52	54.14	4.29	1.03	1.00	0.061
HMBS^{f}	290.112	-20.278	19.71	17.03	22.42	8.01	1.48	1.48	-0.002
ISPA^{i*}	250.656	-27.125	67.35	-6.70	67.16	-9.61	0.30	0.30	0.008
JRGN^{c}	289.425	-23.289	25.91	20.25	28.16	11.31	1.21	1.22	-0.005
KOUR^{i*}	307.194	5.252	-6.46	11.17	-0.92	0.67	0.56	0.53	-0.055
LHCL^{i}	294.405	-38.003	-0.06	10.13	0.57	0.66	0.80	0.79	-0.023
LPGS^{i}	302.068	-34.907	-0.50	11.71	1.30	1.56	0.64	0.64	0.004
MABA^{b}	310.878	-5.362	-3.62	15.14	1.34	4.44	1.14	1.13	-0.019
MCLA^{c}	289.753	-22.746	20.64	17.84	22.99	8.86	1.01	1.01	-0.006
MICA^{f}	290.173	-21.715	24.96	17.79	27.48	8.76	1.21	1.22	-0.004
MNMI^{f}	290.404	-19.131	14.37	17.21	17.25	8.16	1.08	1.08	-0.002
MSCG^{b}	305.459	-20.441	-4.06	11.55	-0.46	1.16	1.08	1.08	-0.002
MTCO^{b}	304.544	-10.804	-4.17	10.50	0.25	0.17	1.54	1.53	-0.007
MZAC^{a}	291.124	-32.895	10.15	13.31	11.18	4.18	1.14	1.14	-0.010
MZAE^{a}	291.850	-33.255	7.03	20.40	8.07	11.19	2.13	1.98	-0.001
MZAS^{a}	291.665	-34.615	3.87	11.19	4.70	2.00	2.13	2.12	-0.003
NAUS^{b}	299.945	-3.023	-4.96	10.99	0.03	1.01	1.04	1.01	-0.003
PB01^{g}	290.512	-21.044	20.57	16.86	23.20	7.80	1.01	1.01	-0.004
PB03^{g}	290.248	-22.049	22.39	17.20	24.86	8.17	1.01	1.01	-0.005
PB04^{g}	289.850	-22.335	24.56	18.75	26.97	9.76	1.12	1.12	-0.004
PCCL^{c}	289.893	-18.458	12.78	16.28	15.72	7.29	1.12	1.12	-0.001
PCHA^{f}	290.568	-19.869	18.68	16.76	21.47	7.69	0.84	0.84	-0.002
PICA^{f}	290.777	-20.503	17.34	14.51	20.06	5.42	0.84	0.84	-0.003
PMEJ^{f}	289.552	-23.101	28.04	19.33	30.33	10.37	1.08	1.08	-0.006
POAL^{b}	308.880	-30.074	-0.35	12.74	2.62	2.15	1.14	1.14	0.002
POVE^{b*}	296.104	-8.709	-4.69	12.86	-0.32	3.22	0.85	0.84	0.004
PSGA^{f}	289.877	-19.597	18.35	16.33	21.14	7.34	1.01	1.01	-0.002
PTRE^{c}	290.426	-18.194	8.39	17.55	11.40	8.50	1.12	1.12	0.000
RADO^{f}	291.073	-22.083	15.19	14.86	17.71	5.74	1.07	1.08	-0.005
RIOB^{b}	292.197	-9.965	-4.04	11.75	0.08	2.50	1.02	1.01	0.006
RIOG^{i*}	292.249	-53.785	3.17	11.87	1.39	2.62	0.47	0.46	-0.011
SALU^{b}	315.788	-2.593	-4.19	11.25	0.97	0.36	1.04	1.03	-0.034
SANT^{i}	289.331	-33.150	20.34	16.33	21.18	7.40	0.77	0.78	-0.025
SAVO^{b}	321.568	-12.939	-5.05	11.00	-0.10	-0.02	1.02	1.04	-0.021
SRGD^{c}	290.652	-22.871	16.79	16.30	19.18	7.22	1.21	1.22	-0.004
TOPL^{b}	311.669	-10.171	-5.24	11.22	-0.54	0.49	1.09	1.09	-0.016
TUCU^{a}	294.770	-26.843	2.05	10.79	4.19	1.28	0.77	0.77	-0.007
UAPE^{f}	289.859	-20.243	20.54	16.49	23.24	7.50	1.01	1.01	-0.003
UCNF^{f}	289.591	-23.679	29.03	19.16	31.24	10.20	1.07	1.08	-0.007
UCOR^{a}	295.806	-31.435	3.21	10.89	4.84	1.28	1.15	1.14	-0.006
UNRO^{a}	299.372	-32.959	1.01	10.52	2.77	0.59	1.14	1.14	-0.003
UNSJ^{a}	291.423	-31.541	8.37	12.11	9.61	2.95	2.12	2.12	0.000
URCU^{f}	289.847	-21.764	25.48	18.26	27.97	9.27	2.12	2.12	0.001
UTAR^{f}	289.703	-18.491	15.49	16.01	18.42	7.04	0.82	0.82	0.000
VALL^{f}	289.236	-28.572	22.74	18.81	24.23	9.89	1.09	1.08	-0.013
VBCA^{a}	297.731	-38.701	2.10	10.80	2.99	1.01	0.79	0.77	-0.013
VLZL^{c}	290.035	-23.117	19.59	16.54	21.90	7.53	1.30	1.31	-0.004

Table 3: Horizontal velocities in mm/yr of permanent stations used to stabilize the processing. Sites used to constrain the reference frame are marked by the * symbol. Stations are either from IGS network ^{i}, French-Chilean network ^{f}, German IPOC network ^{g}, CAnTO (Caltech Andean Tectonic observatory) GPS network ^{c}, RAMSAC Argentine network ^{a}, or RBMC Brazilian network^{b}.

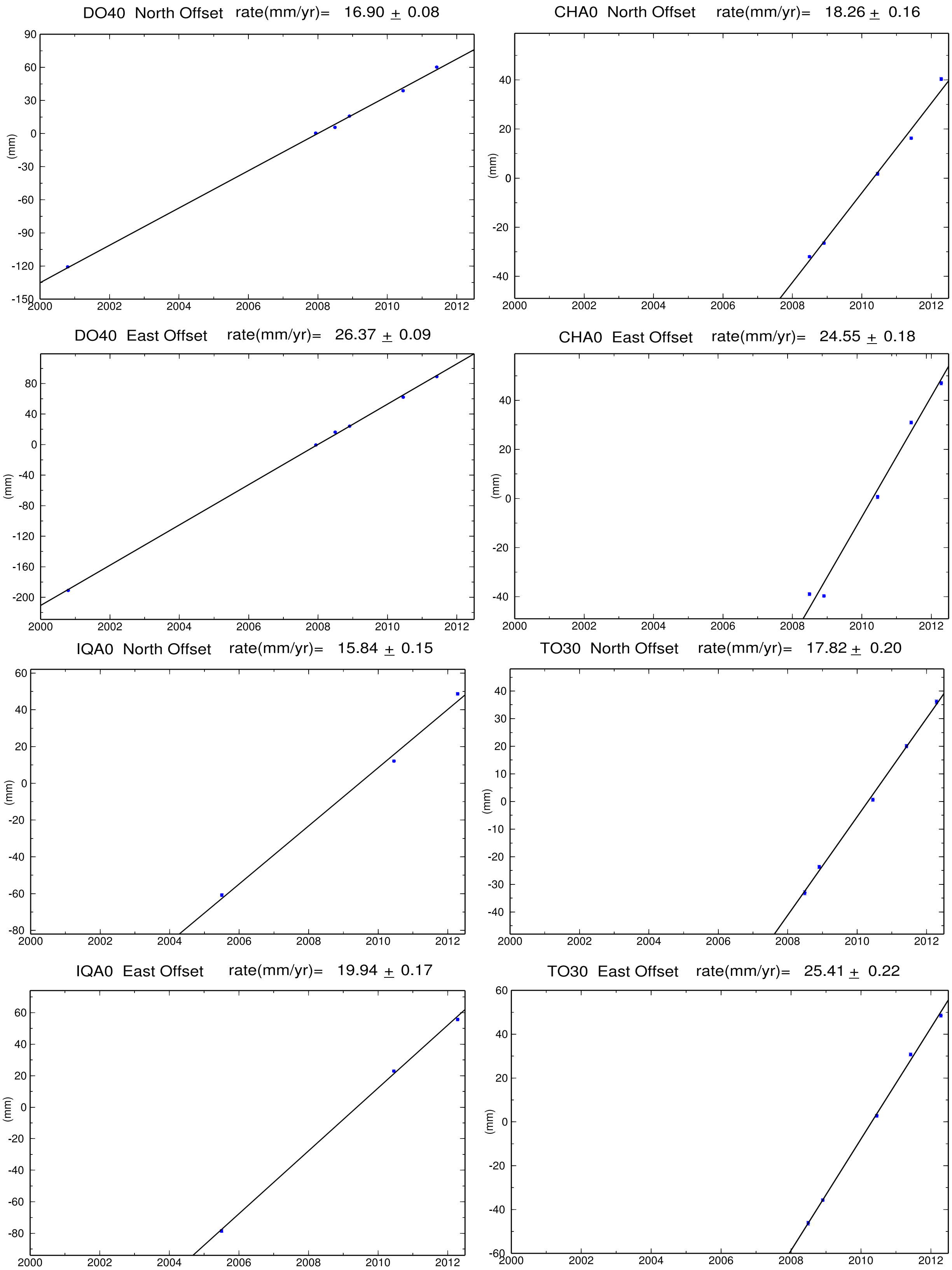

Figure 4: Time series of horizontal components of the interseismic velocity of DO40 (Domeyko profile), CHA0 (Mejillones peninsula), TO30 (Tocopilla profile), IQA0 (Iquique profile).

1.2 Combining with inland data

Brooks et al. [2011] published recently a new GPS data set that quantify the backarc shortening along two East-West profile lines through the subandean fold-and-thrust belt in the central Andes area. These data were collected from 2000 to 2003 and can help greatly in constraining the amount of backarc shortening as 12 measurements are far enough from the main thrust to sample both the stable core of the Andean block and the South American craton, without being impacted by the elastic deformation. In this Auxiliary Material, we invert jointly these data with ours in order to test the validity of our 3-plate models (see Modeling subsection).

However, Brooks et al. [2011] published their interseismic velocities in a South-America fixed unknown reference frame, that complicates the comparison with our data. We use our own data set in the NNR-Nuvel1A fixed South America as the reference and we compute the difference between our values and Brooks et al. [2011]' at common points. We then invert for a rotation pole that minimizes the residuals and apply this pole to the [Brooks et al., 2011] data set. Finally, we find that the pole (3.970°N 102.32°W -0.017°/Myr) produces low residuals at the common reference stations (BRAZ, FORT, KOUR, LPGS). We summarize the final velocities on the 12 points that are on the stable part of both blocks in supp. Table 4.

SITE	Position		Velocity		Uncertainties		r
	Lon.	Lat.	Vlon	Vlat	σ_{lon}	σ_{lat}	
BLSK	295.290	-21.560	8.77	3.75	0.22	0.28	-0.083
CCDO	297.610	-19.430	1.50	1.91	0.81	0.97	-0.168
DRDO	295.650	-19.290	9.31	3.26	0.76	1.19	-0.156
M009	297.110	-21.570	3.36	1.40	1.03	0.66	0.287
M010	297.240	-21.640	0.67	1.20	1.03	0.66	0.287
PBOL	297.370	-21.560	2.25	0.90	0.20	0.16	-0.560
SUCE	294.690	-19.000	7.81	4.44	0.10	0.07	-0.174
SUCR	294.790	-18.990	11.01	1.16	0.77	0.70	-0.012
TARI	294.950	-21.630	10.27	1.15	0.52	0.51	-0.051
TRJA	295.280	-21.540	7.17	1.45	0.25	0.20	-0.293
UYNI	293.170	-20.460	11.76	3.39	0.08	0.08	-0.262
ZDNZ	295.300	-19.120	10.31	3.75	0.81	0.72	-0.089

Table 4: GPS data from Brooks et al. [2011] rotated in the NNR-Nuvel1A South-American fixed reference frame.

1.3 Vertical interseismic motion

We decided in this paper not to use the vertical velocities from our calculation because : (i) early and recent campaigns use different antennae types and important biases can be due to instrumental changes, (ii) the repeatability associated to the vertical component of relative position vectors is more than 3 mm/yr (see supp. Table 1), (iii) time series span only two years on the newest sites, (iii) numerous ties had to be done between the remains of old markers and new ones on the oldest sites; those ties are precise horizontaly but not verticaly.

However, in general terms interseismic vertical velocities provide valuable information that helps constraining the downdip limit of the highly locked zone, with little dependence to the reference frame issues and the block motion amount. We show the vertical motion pattern based on stations with more than 2 years of data in supp. Figure 5. The general pattern of our preliminary interseismic vertical velocities underlines the fact that very few points are subsiding while the bulk of the data shows uplift of more than 3 mm/yr (a resolvable motion at 1σ). Among the subsiding points, two of them are campaign points of the Iquique profile that are very close to permanent sites that are registering uplift. Therefore, we don't trust these measurements. The two remaining subsiding points are permanent

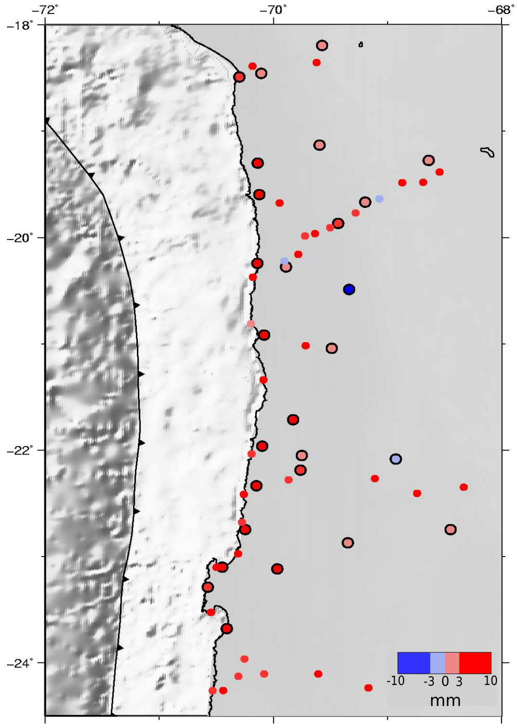

Figure 5: Vertical interseismic motion on the c-GPS network (bold contoured dots) and s-GPS campaign benchmarks that were measured at least twice over more than a two years time span. Subsidence (blue) and uplift (red) are color-coded.

stations PICA and RADO that are located in an oasis and a mining area respectively. Therefore, it is very probable that human activities of pumping or mining influence the vertical motion of those stations. The general pattern of our data is supported by recent Insar data processed in the area that show uplift of the whole area, with maximal uplift near the coast [Béjar-Pizarro et al., 2013].

Referring to these data, the whole North Chile is uplifted during the interseismic loading phase.This regional uplift would imply that the highly coupled zone can not extend far under the continent [Savage, 1983]. We will wait for longer time series and a more precise determination of the vertical velocities before we formally include them in our modeling.

2 Technical choices for modeling

The inversion procedure of the best model presented in Figure 4 is conducted using 264 independent observations to determine 207 (3-plate model with zero coupling below 80 km depth) or 204 parameters (2-plate model with zero coupling below 80 km depth).

2.1 Slab geometry

The geometry of the plunging plate in North Chile has been explored by the ANCORP [2003] tomography study but is still poorly known. Recently, Peyrat et al. [2010], Contreras-Reyes et al. [2010] and Fuenzalida et al. [2013] used relocated seismicity following the Mw 7.7 Tocopilla earthquake to assess the precise slab geometry North of Mejillones peninsula. They demonstrate that the slab steepens at 30 km depth from $\sim$18° to $\sim$25°, forming a kink in the interface. However, in this study, we prefer to use a simple planar geometry adapted to the backslip assumption. As others did [e.g. Chlieh et al., 2011], we tried to constrain the dip of the slab using our GPS data set. We thus invert for coupling distribution using different dip values ranging from 10° to 30°, with a 0.7 smoothing coefficient linearly increasing with depth, and without sliver block motion. Logically, we observe that the amount of coupling on the shallow subduction interface increases with the dip of the slab, but that similar lateral variations are observed regardless of the slab geometry. The results are presented in supp. Figure 6. We conclude from these tests that it is difficult to invert for the slab geometry using our GPS measurements, as we can not discriminate between 12° and 24° dipping slabs on the base of the nRMS. Therefore, we adopt an average value of 20° for the slab geometry, also used by Chlieh et al. [2004] and coherent with the geophysical and seismological studies in the area.

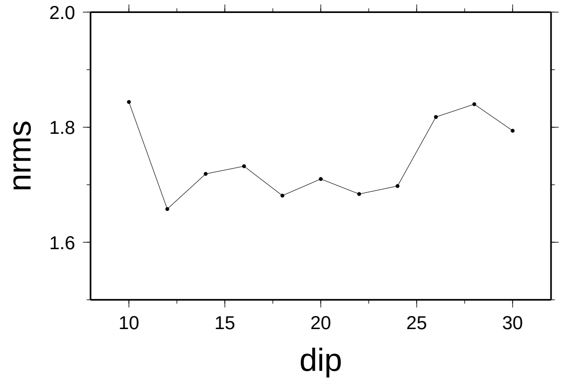

Figure 6: Normalized RMS versus dip of the slab in °.

2.2 Sensitivity and resolution

We calculate the sensitivity of our network to unit displacement on each node of the grid by summing the horizontal deformation on the whole network as suggested by Loveless and Meade [2011] (see supp. Figure 7). Logically, the "power" of our network to constrain the coupling on the interface is high under the area where our network is dense. This is particularly true for the Iquique zone that extends from 21°S to 19°S. There, the sensitivity is high even for nodes located below 80 km depth. However, such deep coupling on the interface is quite unlikely but impacts the predicted vertical deformation pattern. Thus, we impose zero coupling for depth larger than 80 km. The sensitivity is

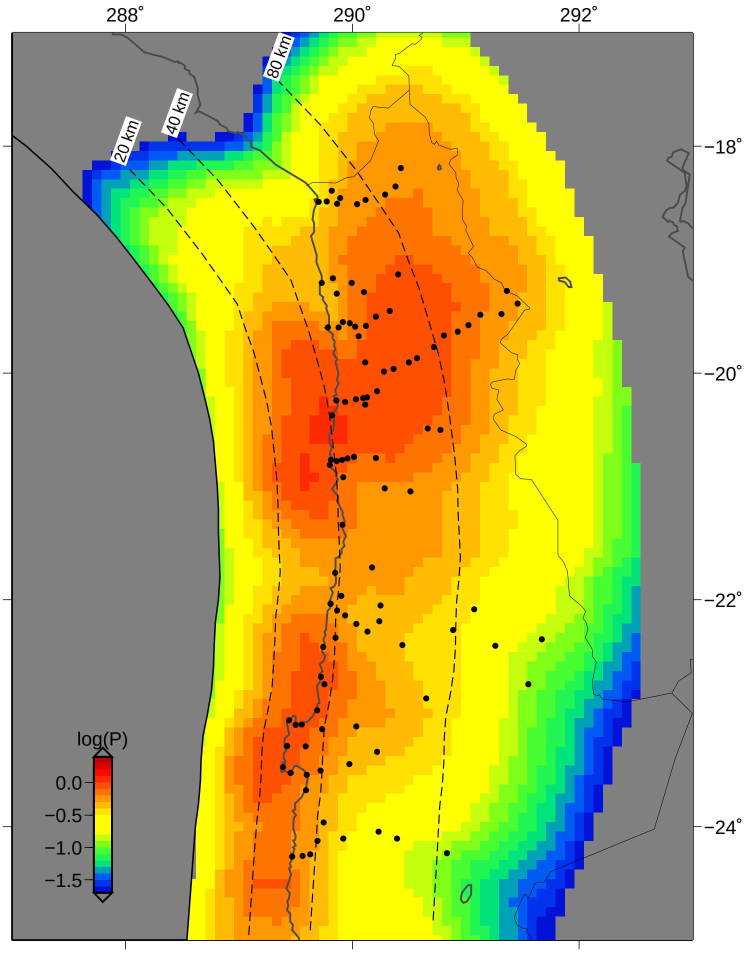

Figure 7: Sensitivity of our network to unit coupling on the 20° dipping slab. Each element of the interface is colored by the log of the sum of the displacements (P in mm/yr) at GPS stations (dots) due to unit slip on the nearest grid node.

high in general along the coast (level at which the slab is ∼40km depth), but the sensitivity to coupling slightly decreases around 21.5°S because our network is locally sparse. The sensitivity to shallow nodes is low in general and coupling between 0 and 10 km depth is thus poorly constrained, except in front of the Mejillones peninsula where the coastal points are closer to the trench than usual (90 km). This is why constraining the coupling value on these nodes to 0% or 100% does not impact the nRMS of the inversion (see supp. Figure 15). Imposing zero coupling down to 10 km depth in front of the Mejillones peninsula and in the Antofagasta region generates systematic eastward-pointing residuals (see supp. Figure 15). Therefore, we do have resolution to constrain shallow coupling coefficient in this area. The sensitivity decreases strongly on the network edges, in particular close to the Chile-Peru border (North of 18.3°S) where the distance between the coast and the trench increases to 150 km and because we lack measurements in South Peru.

Usual checkerboard tests presented in supp. Figure 8 confirm that our network is able to picture accurately variations of the coupling coefficient both along-strike and along-dip if located on the subduction interface between 10 and 80 km depth.

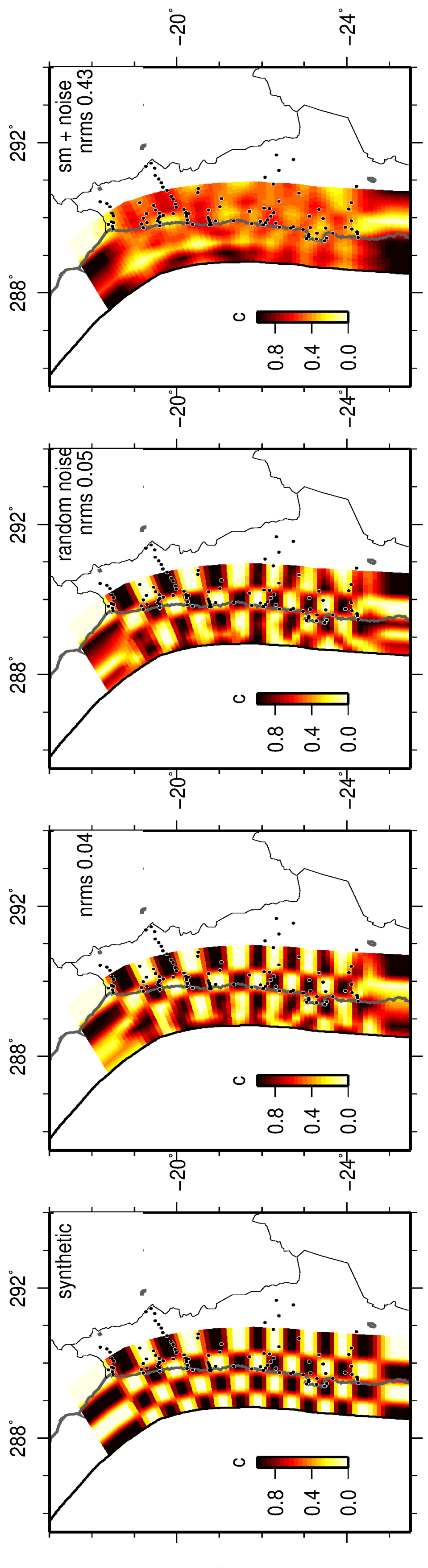

Figure 8: Checkerboard resolution tests. From left to right : coupling checkerboard pattern used to generate a synthetic deformation field; coupling distribution retrieved by an inversion of the raw synthetic velocities without smoothing constrain; coupling distribution retrieved by the inversion of the synthetic velocity field in which random noise has been added; same but adding an homogeneous smoothing constrain (0.7/°) which smears the small scale original checkerboard.

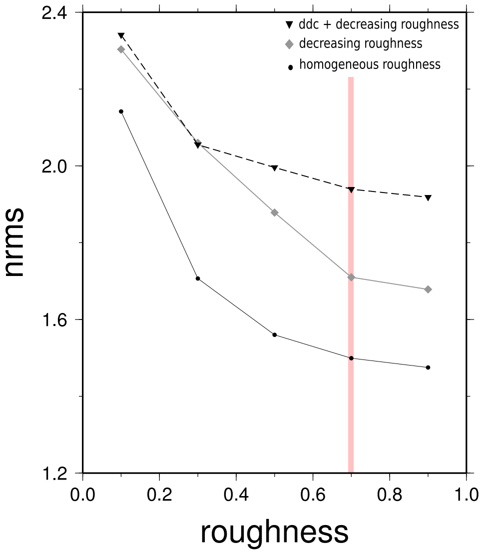

Figure 9: Normalized RMS for homogeneous roughness (plain black line), decreasing roughness with depth (i.e. increasing smoothing, plain grey line), and down-dip decrease option with decreasing roughness with depth (dashed black line), versus roughness (in /°).

2.3 Smoothing constrain

We test two smoothing options that are implemented in Defnode (homogeneous "sm" or increasing with depth "smz") in order to reduce numerical instabilities and unrealistic deep coupling patches. We quantify the smoothing amount by fixing in the program the allowed roughness of the coupling distribution, given in maximal coupling variation by degree of latitude (/°). Therefore, using the "smz" option imposes a linear increase of the smoothing with depth equivalent to an along-dip decrease in the roughness amount.

We plot the normalized RMS associated to data versus roughness amount (i.e. the opposite of smoothing) in supp. Figure 9. We also combine the increasing smoothing option "smz" with the down-dip decrease option (or "ddc") that constrain the coupling coefficient to decrease with depth along one column of nodes. In the following, we prefer to use the "smz" option with a 0.7/° surface roughness, as it yields the best compromise between smoothing and nRMS (i.e no significant improvement of the nRMS is obtained using higher roughness coefficient, see figure 14). However, note that we do not impose smoothing in the along-dip direction since it was not implemented in the 2007 Defnode version. Thus we have small variations in the amount of coupling in the same column of nodes that are artifacts of the modeling process.

2.4 Nazca-South America relative motion

The direction and amplitude of the Nazca-South America convergence motion have been extensively debated for years [e.g Norabuena et al., 1998, DeMets Gordon, 1994, Kendrick et al., 2003, Vigny et al., 2009]. This uncertainty is mainly due to the non-negligible discrepancy that exists between the geological velocity calculated by the Nuvel 1-A model for the Nazca plate [DeMets Gordon, 1994] and the ones derived using present-day GPS measurements [Norabuena et al., 1998, Kendrick et al., 2003, Vigny et al., 2009]. Both calculations lead to velocities that differ by nearly 15%. This could be the result of a decrease in the convergence velocity between both plates since 3 Myr. The more recent ‘geological” model using a shorter time span of 0.76 Myr (MORVEL) [DeMets et al., 2010] falls halfway between Nuvel 1-A and GPS values [Altamimi et al., 2011] and concur with this idea of a progressive slowing down of the convergence. We summarize in table 5 some of the poles that have been proposed to describe the Nazca-South America motion.

Model	source	rotation pole	⟨velocity⟩
	(N,E,°/Myr)	(mm/yr)	
Nuvel 1-A	[DeMets Gordon, 1994]	56.0 -94.0 0.720	77
MORVEL	[DeMets et al., 2010]	54.9 -98.0 0.666	73.3
GPS1	[Norabuena et al., 1998]	47.4 -93.7 0.624	66.7
GPS2	[Kendrick et al., 2003]	61.0 -94.4 0.570	63
GPS3-this study	[Vigny et al., 2009]	55.9 -95.2 0.610	67
ITRF 2005	[Altamimi et al., 2007]	53.9 -87.5 0.605	66.1

Table 5: Summary of published poles for the Nazca-South America relative motion using either geological methods (top) or GPS velocities only (bottom). The average velocity predicted by each pole at 24°S (i.e the center of our study area) is indicated in the last column (in mm/yr).

In our modeling, we do not invert for the relative motion between Nazca and South American plate. In our best models, we chose to use the pole calculated by Vigny et al. [2009] using GPS measurements in central Chile (55.9°N, 95.2°W, 0.610 °/Myr) that is quite similar to the ITRF rates (±1mm/yr) and slightly lower than the MORVEL rate (-6mm/yr). Because a trade-off exists between the value of the convergence between both plates and the amount of coupling on the subduction interface, we tested the impact on our inversion of using the alternative poles presented in supp. Table 5 (see Alternative models section).

3 Alternative models

3.1 Bimodal models

We tested bimodal simple coupling distributions in forward tests as previously done by Chlieh et al. [2004, 2011]. In those runs, we impose a fully coupled zone ($\Phi = 1$) that extends from surface to a locking depth z, below which we impose a 20 km wide transition zone above the freely creeping deep interface where Φ is zero. We test for variable locking depths in order to determine a first-order coupling pattern (see supp. Figure 10), and find that the best bimodal model is obtained for a downdip limit of the locked zone located between 50 and 55 km depth. This is 10 km deeper than the best bimodal model proposed by Chlieh et al. [2011], but this may be due to the fact that he uses a 18° dipping slab in this region. However, our "preferred" bimodal model is not satisfactory as the fit to the data is not optimal and residuals are systematics along the entire network (see supp. Figure 11). Residuals that are pointing trenchward in the Mejillones peninsula suggest that coupling is higher than needed in reality. On the other hand, eastward pointing residuals in the inland part of the Iquique profile indicate that a large-scale eastward motion is taking place there, potentially the rigid rotation of the Andean bloc. Those significant residuals demonstrate that a simple bimodal model is not sufficient to reproduce the data and that lateral variations of the coupling are needed.

We also explored those bimodal models in a 3-plate configuration (i.e. inverting for the motion of the rigid Andean sliver) for various locking depths. In general and logically, adding a sliver motion increases the fit to the data (see supp. Figure 10). However, even with the "best" 3-plate bimodal model obtained for a 20 km locking depth, we get systematic residuals in the Iquique and Mejillones areas that illustrate the need of lateral variations of the coupling (see supp. Figure 12).

3.2 2-plate alternative models

We conducted several inversions of the coupling distribution in the case of a simple convergence between the Nazca plate and the South-American plate. For many of them, the normalized RMS is higher than 1.8, with systematic residuals, and the coupling distributions are either patchy or with very deep highly coupled zones. This convince us that such a 2-plate description could not reproduce our data. Among all the models we tested, the most coherent ones are the inverted coupling distributions

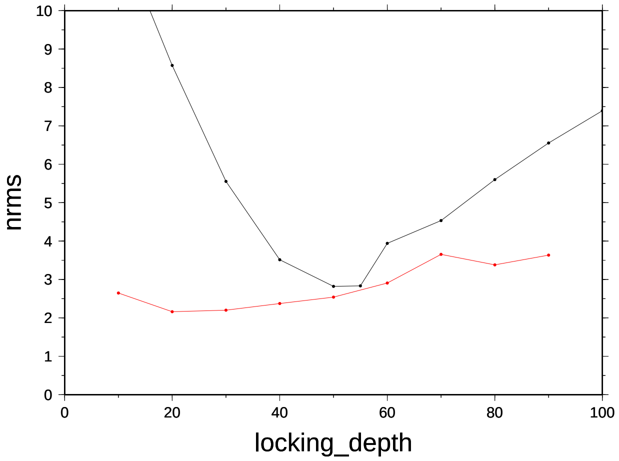

Figure 10: Normalized RMS versus depth of the downdip limit of the locked zone in km for 2-plate (black curve) and 3-plate (red curve) configurations.

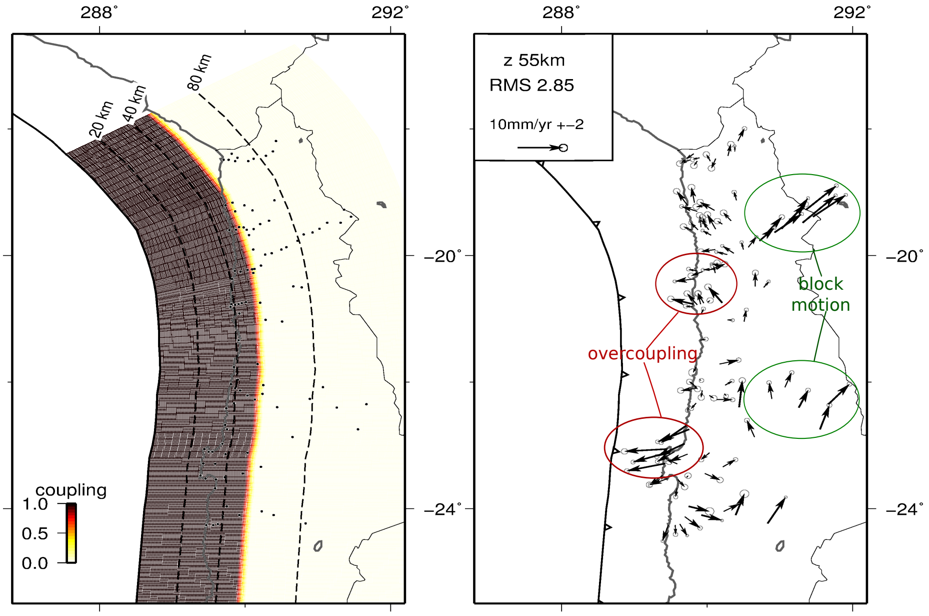

Figure 11: Right : best bimodal coupling distribution for z=55 km. Left : associated residuals.

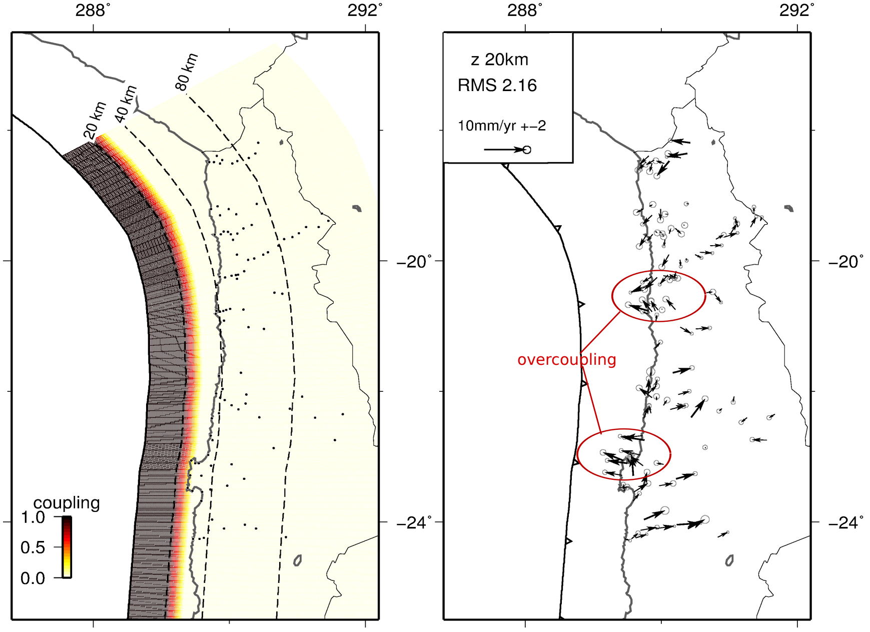

Figure 12: Right : best 3-plate configuration bimodal coupling distribution for z=20 km. Left : associated residuals.

presented in supp. Figure 13 where the smoothing coefficient is set to 0.7/°. Imposing or not the down-dip decrease constraint on the coupling does not impact the nRMS, but models in which non-zero coupling is allowed below 80 km depth improve the fit to the data. Models in which coupling is allowed to increase with depth differ from the “ddc” constrained models mainly by a deep highly coupled patch under the Iquique coast (20°S). We prefer to present in the main text the model from supp. Figure 13c where deep coupling is fixed to zero, as it picks up the main trends of all the 2-

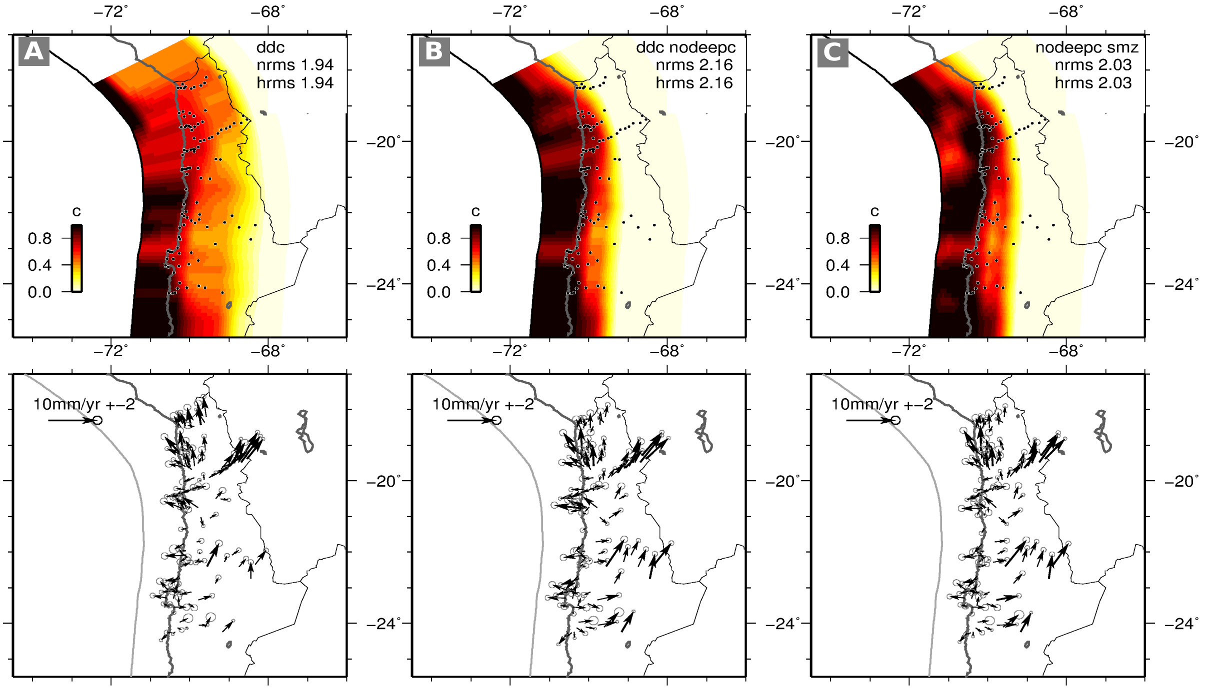

Figure 13: Examples of coupling distributions obtained using a simple 2-plate kinematic for the convergence (top row) and associated residuals (bottom row). A- Model obtained using down-dip decrease option; B- same than A but with coupling fixed to zero down 80 km depth; C- ‘best” coupling distribution obtained without down-dip decrease constrain but with zero coupling down 80 km depth. All inversions were conducted with a 0.7/° smoothing coefficient increasing with depth.

plate models. However, all those preferred 2-plate models, even the models in which deep coupling is allowed and that are thus artificially able to reproduce part of the far-field eastward motion, produce large residuals in the northern part of our network pointing toward the East. This emphasizes the presence of a sliver motion in North Chile.

3.3 3-plate alternative models

Since the publication of the first interseismic velocities in the North Chile-South Peru area of the Nazca subduction zone, Norabuena et al. [1998] proposed that a certain amount of the convergence between the Nazca and South American plate is taken up by crustal shortening localized at the front of the subandean fold-and-thrust belt. They estimated a 10-15 mm/yr shortening rate there and proposed a relative rotation pole between Nazca and South American plate that has been confirmed since then. On the other hand, Bevis et al. [2001] used an ad-hoc combination of their own data set with the data from Norabuena et al. [1998] and found that full coupling between 10 and 50 km depth on the interface and only 5-6 mm/yr of backarc shortening were necessary to explain the interseismic GPS velocities. Recently, Brooks et al. [2011] published new measurements along two profile lines across the Bolivian orocline and conclude that 9-13 mm/yr of shortening are accumulated there. Therefore, backarc shortening rate estimates are still poorly known with major consequences on the seismic potential assessment of the backarc region. In this study, we roughly define the Eastward limit of the Andean sliver block as the eastern Andes topographic scarp (see Fig. 2 in the main text), and consider that the backarc shortening can be modeled using a rigid block motion hypothesis. Then, we invert simultaneously for the Andean sliver motion and for the coupling distribution on the subduction interface. Because even small amount of very deep coupling are quite unrealistic and may strongly affect the predicted surface deformation, we impose zero coupling below 80 km depth in all 3-plate models.

We present in supp.Figure 14 the coupling distributions and associated residuals inverted for varying "smz" roughness coefficient, and list in table 6 the associated Eulerian poles between the Andean sliver and the stable South America.

roughness (/°)	nRMS	rotation pole (N,E,°/Myr)	⟨rot⟩ (mm/yr)
0.1	2.37	28.68 270.38 0.212	18.93
0.3	1.71	-67.05 357.07 -0.148	14.49
0.5	1.53	-56.60 323.55 -0.159	12.10
0.7	1.45	-54.50 322.51 -0.148	10.87
0.9	1.42	-57.09 330.81 -0.126	10.18

Table 6: Normalized RMS, Andean sliver pole and average horizontal motion produced by block rotation on the entire network, depending on the roughness coefficient "smz" imposed in our 3-plate models presented in figure 14.

Except for the smoothest models (0.1 and 0.3 roughness coefficient "smz" which mimics bimodal models), the nRMS is lower or equal to 1.5 and the residuals are no more systematic. All models share the same pattern of interseismic coupling : on average, coupling decreases from South to North of the network. Two low average coupling zones (in front of Mejillones and Iquique) separate three highly coupled shallow patches, and coupling tends to deepen beneath Iquique. All models except the smoothest ones are used to define the segments and intersegment areas in Fig. 5 of the main text. In these models, the sliver pole is located far away in the Southern Hemisphere and the rotation rate generates a convergence rate lower than 13 mm/yr on average over the entire network. The sliver motion is very similar to an homogeneous north-eastward translation, but with slight decrease from North to South of our network.

constrain	NRMS	rotation pole (N,E,°/Myr)	⟨rot⟩ (mm/yr)
0.7 z	1.42	-54.50 322.51 -0.148	10.87
0.7 z + ddc	1.48	-51.96 316.64 -0.176	11.76
0.7 z + lock1	1.44	-48.61 312.21 -0.19	11.45
0.7 z + lock2	1.46	-45.26 308.89 -0.21	11.17

Table 7: Normalized RMS, Andean sliver pole and average horizontal motion produced by block rotation on our network, depending on the constrains imposed in our 3-plate models (figure 15).

We then tested the effect of the downdip decrease constrain ("ddc"), and of superficial locking or unlocking with "smz" equal to 0.7 (see supp. Figure 15). All those models fit well the data (nRMS$\sim$1.4) with similar estimates of the sliver motion (see supp. Table 7). This variability in the best models is used to define the segmentation of the margin based on the along-strike variations of the average coupling $\langle\Phi\rangle$ (see Fig. 5 in the main text). As presented is supp. Table 7, the average horizontal motion of the sliver is around 11 mm/yr (±0.7) for our preferred models. This value is coherent with Norabuena et al. [1998]'s and Brooks et al. [2003]'s estimates. However, an important trade off exists between the amount of coupling on the interface and the amount of backarc shortening on the subandean fold-and-thrust belt. We thus invert for the coupling distribution while fixing the

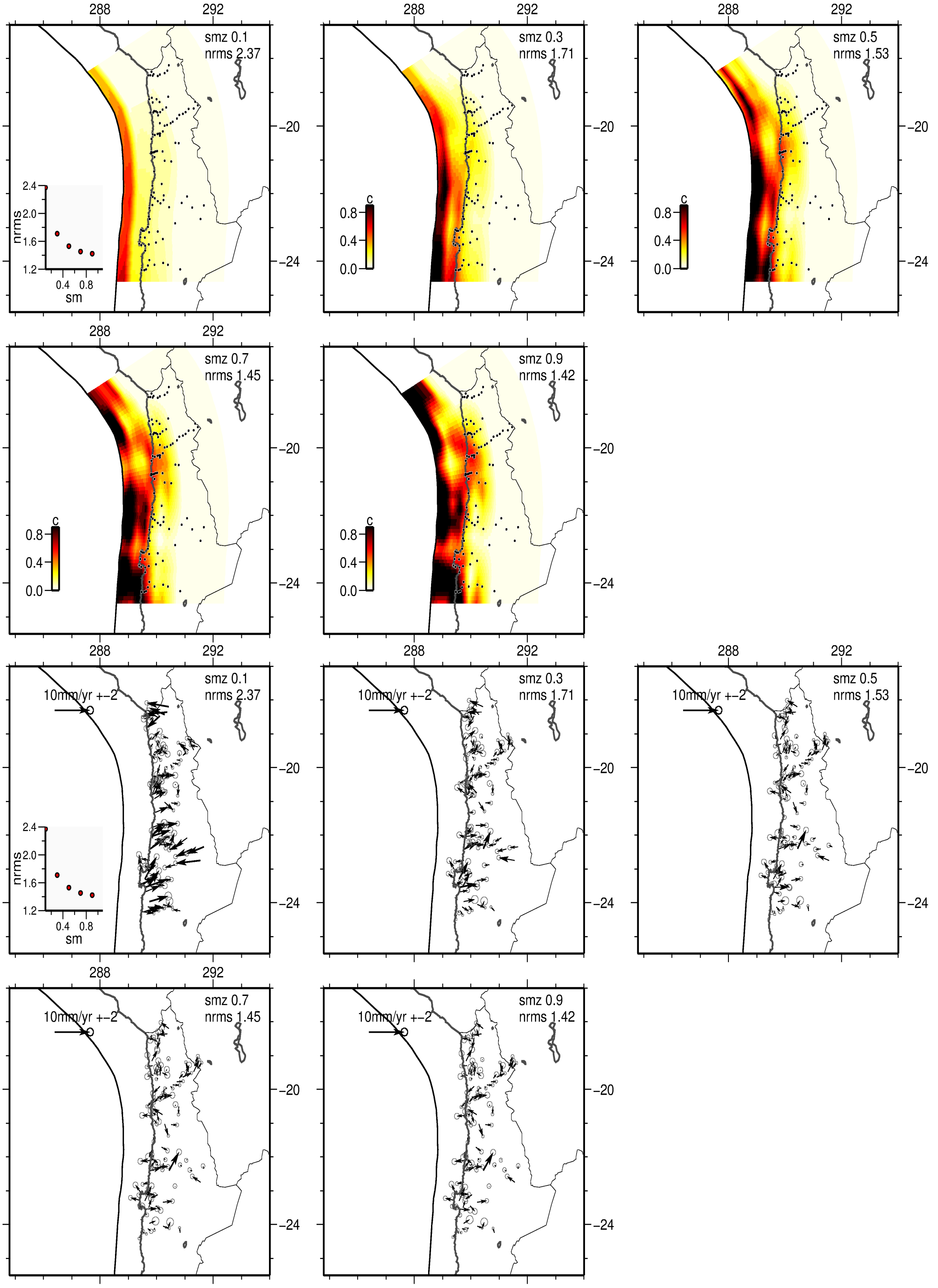

Figure 14: Top : coupling patterns inverted for a 3-plate model using different values for the smoothing coefficient, and inverting for the Andean sliver block motion. Smoothing coefficient varies from 0.1 to 0.7°. Bottom : residuals associated to the coupling distributions presented above. The smoothing coefficient and the normalized root mean square relative to data (nRMS) are indicated in the upper right corner of each plot. We plot the variations of nRMS with rotation rate in the bottom left corner of the smoothest inversion

Andean sliver Eulerian pole to (-54.50°N, 322.51°E), with varying rotation rates (see supp. Figure 16). The best fit is obtained for rotation rates higher than 0.1°/Myr, and no systematic residuals are observed. There is no significant change of the coupling pattern while increasing or decreasing this rotation rate, but we do observe a decrease of the amount of average coupling when the Sliver motion increases as underlined by Chlieh et al. [2011].

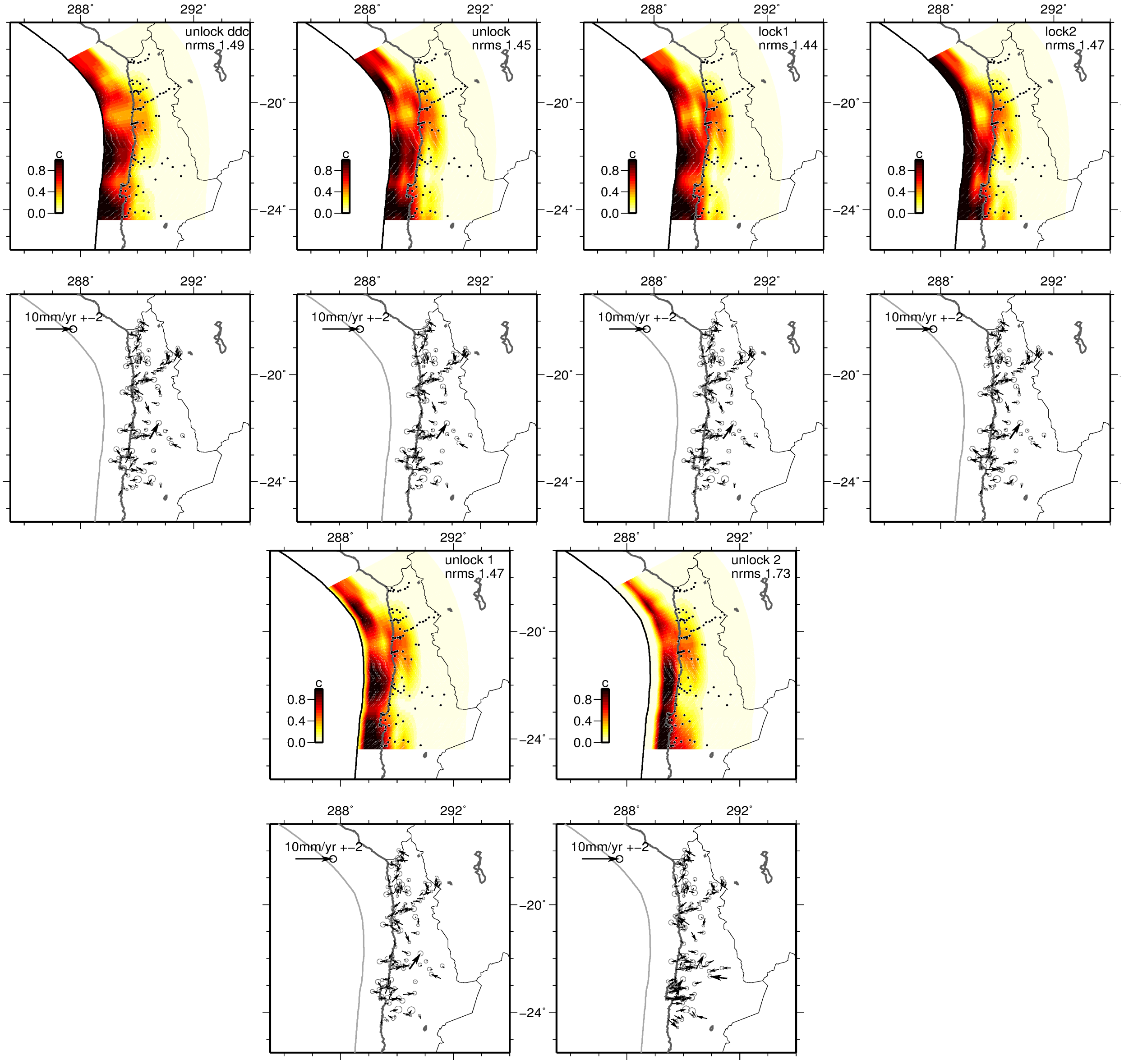

Figure 15: Coupling patterns inverted for a 3-plate model and with different constrains on the shallow coupling. The smoothing coefficient is fixed to 0.7/°, and no coupling is allowed under 80 km depth. From left to right : no constrain on coupling, “ddc” constrain on the coupling coefficient, locking of the surface node only, locking of the whole interface from 0 to 10km depth. Bottom : zero coupling is imposed on the surface nodes only (left) or from surface to 10km depth (right). The normalized root mean square (nRMS) is indicated in the upper right corner of each plot.

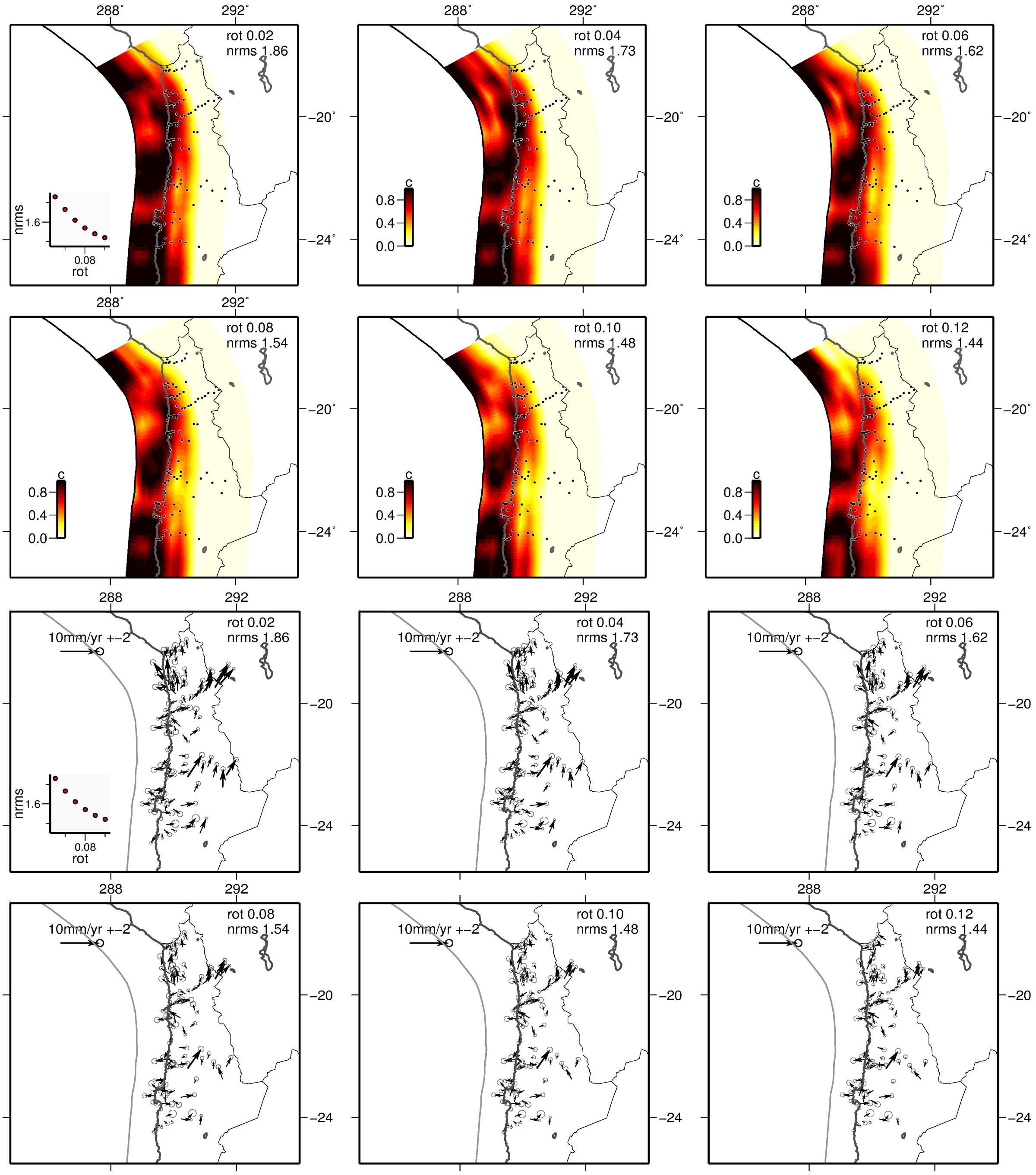

Figure 16: Same caption as figure 14, but for fixed sliver motion rates (from 0.02 to 0.12 °/Myr) around the (-54.50°N, 322.51°E) Eulerian pole (i.e the pole inverted for 0.7/° smoothing coefficient and no superficial locking).

3.4 Influence of complex geometry on coupling

We present in supp. Figure 17 the coupling distribution inverted with the slab geometry proposed by Contreras-Reyes et al. [2012] around the Mejillones peninsula, with 0.7/° decreasing with depth roughness coefficient, and impeded coupling below 80 km depth. This geometry has an abrupt change of the slab dip angle from 10° to 22° at 30 km depth. No obvious change is observed in the lateral variations of the coupling coefficient (we still see the 3 highly coupled segments separated by the 2 weakly coupled intersegments at Mejillones and Iquique), but coupling is overall lower than in our preferred 3-plate model. The usage of this geometry imposes a higher rotation rate around the Eulerian pole of the sliver located at (65.2°S, 348.9°E) and produces an eastward motion of 14 mm/yr on average over the entire network. Therefore, the slab geometry used in our inversion is important to precisely determine the slip deficit accumulated during the interseismic period on the subduction thrust but has a limited impact on the coupling segmentation.

3.5 Compatibility with regional GPS data sets

In order to test whether this $\sim$ 11 mm/yr shortening amount is realistic, we include in the inversion recent inland data from Brooks et al. [2011] rotated in our reference frame (see section 1.2). The coupling distribution is very similar to the models obtained without these inland data (see supp. Figure 18) and the sliver block rotation produces an eastward displacement of 10.7 mm/yr on average over our network.

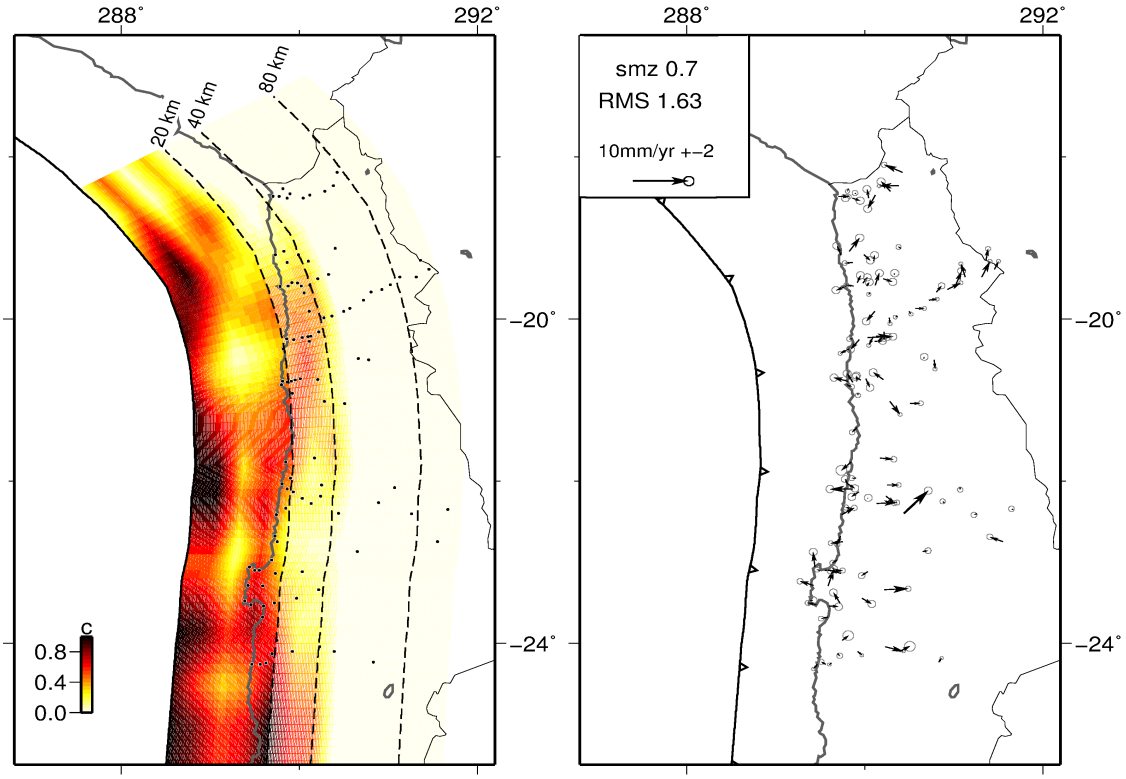

Figure 17: Coupling distribution inverted using the complex slab geometry proposed by Contreras-Reyes et al. [2012], with 0.7/° smoothing coefficient that increases with depth and no coupling allowed under 80 km depth. Residuals associated to this coupling distribution are shown on the right, together with the nRMS value.

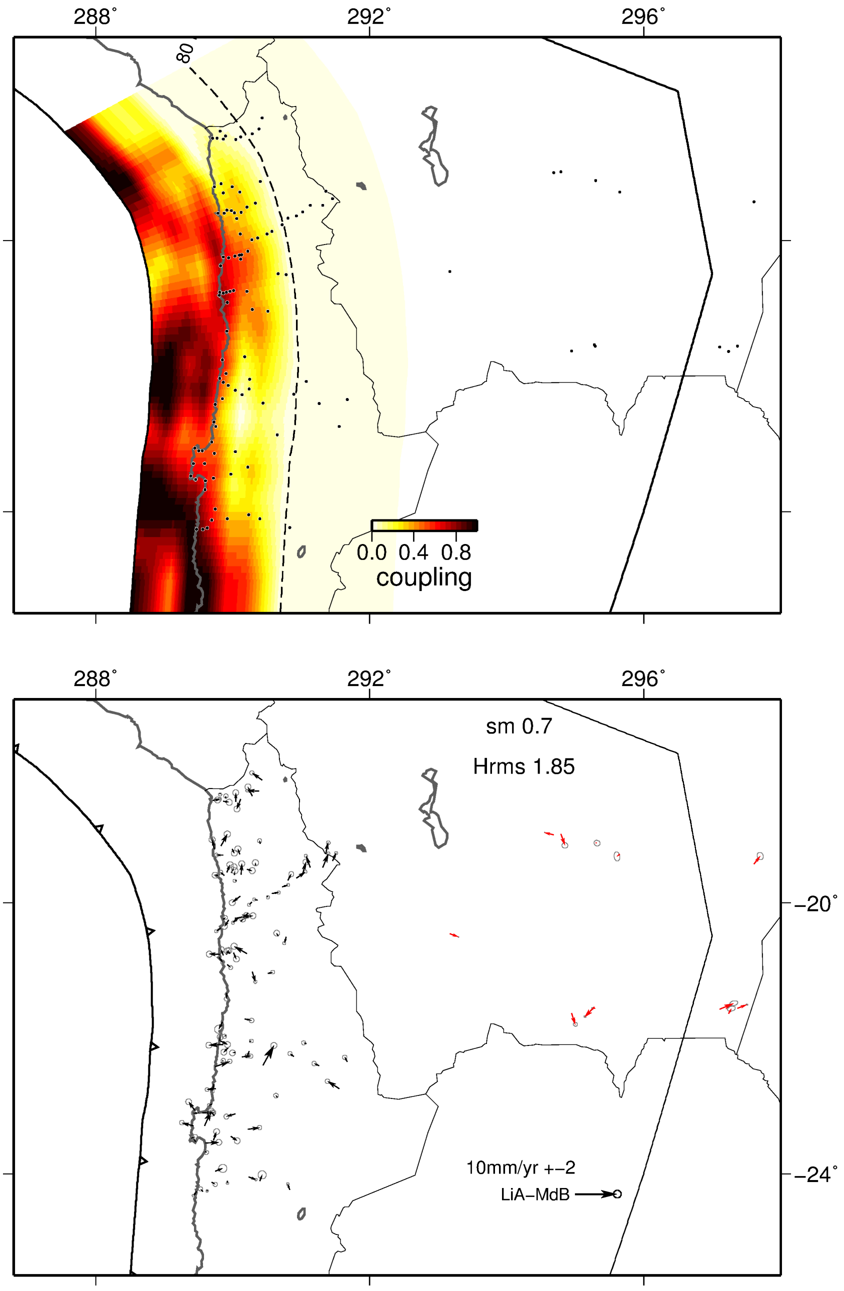

Figure 18: Up: coupling distribution inverted using our own data set and the data from Brooks et al. [2011]; “smz”=0.7/°, without constrain on shallow locking, and with zero coupling under 80 km depth. Bottom : residuals associated to our data set (black) and Brooks et al. [2011] data (red).

3.6 Influence of relative plate motion on coupling distribution

We present in supp. Figure 19 the coupling distributions inverted using other published values for the Nazca-South America convergence motion (see table 5). We tested the pole proposed by Kendrick et al. [2003] that yields the smallest convergence velocity in North Chile (63 mm/yr) and the Morvel pole [DeMets et al., 2010] that is the most recent geological estimate of the convergence (73 mm/yr). We find that fixing the rotation between Nazca and South-American plates to a higher or lower conver-

Pole used	$\langle$convergence$\rangle$ (mm/yr)	NRMS	sliver rotation pole (N,E,°/Myr)	$\langle$rot$\rangle$ (mm/yr)
Vigny et al. [2009]	68	1.451	-54.50 322.51 -0.148	10.87
Kendrick et al. [2003]	63	1.41	-41.09 307.49 -0.234	10.90
MORVEL	73.3	1.55	-65.85 352.30 -0.116	11.14

Table 8: Average convergence between Nazca and South America, normalized RMS, Andean sliver pole and average horizontal motion produced by block rotation on our network, depending on the Nazca-South American relative pole imposed in our 3-plate models (figure 19).

gence rate than 68 mm/yr (estimated from Vigny et al. [2009]) does neither change the details of the coupling distribution on the subduction interface, nor the amount and direction of the inverted sliver motion (see table 8). In particular, the lateral variations of the coupling are very similar : this gives us confidence in the fact that the lateral segmentation is a stable feature. However, logically, we observe that the slower the convergence, the higher the inferred average coupling and the deeper the highly coupled zones. Therefore, we conclude that if the lateral segmentation of the coupling coefficient is little dependent on the convergence velocity, the amplitude and the depth of the highly coupled zone vary with it. This is why we believe we should be very careful with the interpretation of the in-depth variation of the coupling coefficient and with integrated seismic potential accumulation rates on each segments.

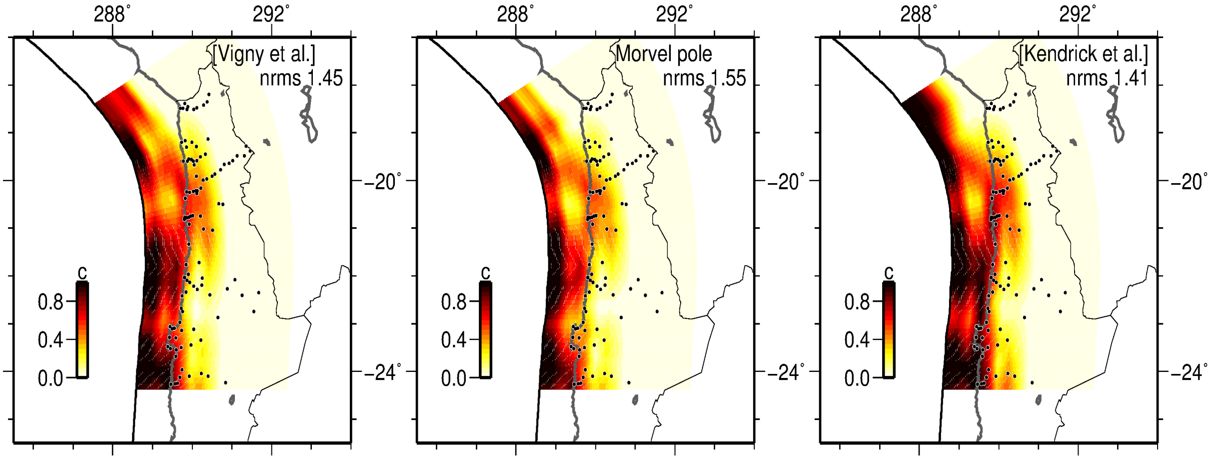

Figure 19: Coupling distribution inverted using various Nazca-South America convergence velocities, with 0.7/° smoothing coefficient that increases with depth, no coupling allowed under 80 km depth, in a 3-plate configuration. From left to right : coupling distribution obtained with Vigny et al. [2009], MORVEL [DeMets et al., 2010] and Kendrick et al. [2003] poles.

3.7 Compatibility with vertical data sets

We show the fit of our preferred model (vertical data were not included in the inversion) to the vertical velocities of continuous GPS stations (supp. Figure 5) on four profile lines normal to the trench (supp. Figure 20). In agreement with the data, our best model predicts uplift almost everywhere but in the northernmost coastal area (profiles c and d in supp. Figure 20). This local misfit is higher for the coupling distribution where deep coupling is allowed, since the vertical elastic deformation is very sensitive to the width of the intermediate coupling area (i.e. the transition zone beneath the highly locked zone). Therefore, the misfit of our model to vertical trends there could be due to overestimation of the width of the downdip transition zone. The joint inversion of both horizontal and vertical velocities at cGPS stations shows a very similar coupling distribution, and the fit to horizontal data is slightly decreased. This might be an indication of a given level of incompatibility between horizontal and vertical data in the framework of elastic modeling. However, it should be noted that vertical data are affected by high uncertainties and possible biases. They should be used with caution. Deformation depicted by Insar data may help constraining the uplift pattern [Béjar-Pizarro et al., 2013].

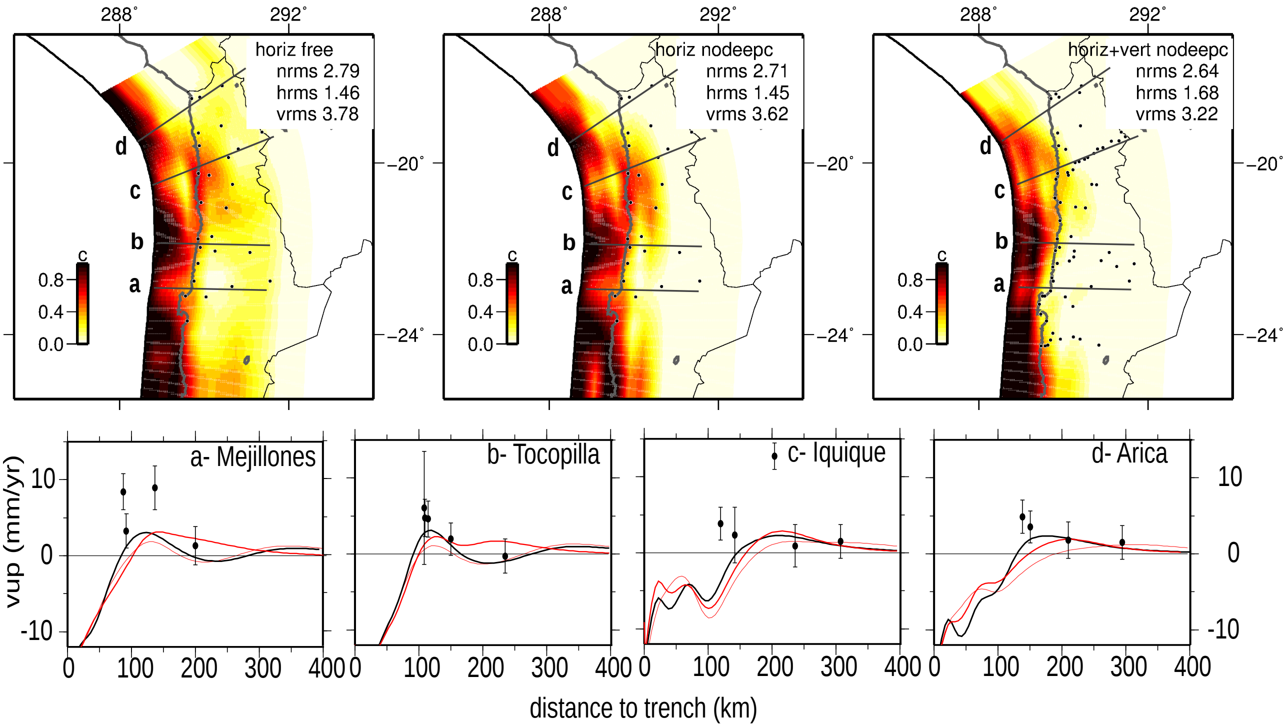

Figure 20: Up, left : coupling distributions inverted using only horizontal data for increasing with depth smoothing of 0.7 and with full locking imposed on the most superficial nodes. Center : same but with coupling set to zero below 80 km depth. Right : coupling distribution obtained with deep coupling set to zero and including both horizontal and vertical velocities presented in supp. Figure 5. The normalized RMS relative to horizontal (hRMS), vertical (vRMS) and whole data set (nRMS) are indicated in the upper right corner of each plot. Dots are permanent stations where vertical velocities are available. Bold gray lines mark the four profile lines. Bottom : vertical deformation (in mm/yr) against distance to the trench plotted along four normal to the trench profile lines predicted by the three models presented above (from left to right : light red, bold red and black lines). Black dots : velocities observed at permanent stations.

References

Z. Altamimi, X. Collilieux, J. Legrand, B. Garayt, and C. Boucher. ITRF2005: A new release of the International Terrestrial Reference Frame based on time series of station positions and Earth Orientation Parameters. *Journal of Geophysical Research*, 112(B9):B09401, 2007. ISSN 0148-0227.

Zuheir Altamimi, Xavier Collilieux, and Laurent Métivier. Itrf2008: an improved solution of the international terrestrial reference frame. *Journal of Geodesy*, 85(8):457–473, 2011.

Working Group ANCORP. Seismic imaging of a convergent continental margin and plateau in the central andes (andean continental research project 1996 (ancorpâĂŹ96)). *J. geophys. Res*, 108(B7), 2003.

M. Béjar-Pizarro, A. Socquet, R. Armijo, D. Carrizo, J. Genrich, and M. Simons. Interseismic coupling and Andean structure in the North Chile subduction zone. *in press to Nature Geoscience*, 2013.

M. Bevis, E. Kendrick, R. Smalley Jr, B. Brooks, R. Allmendinger, and B. Isacks. On the strength of interplate coupling and the rate of back arc convergence in the central Andes: An analysis of the interseismic velocity field. *Geochemistry Geophysics Geosystems*, 2(11):1067, 2001. ISSN 1525-2027.

B.A. Brooks, M. Bevis, R. Smalley Jr, E. Kendrick, R. Manceda, E. Lauría, R. Maturana, and M. Araujo. Crustal motion in the Southern Andes (26–36 S): Do the Andes behave like a microplate? *Geochemistry Geophysics Geosystems*, 4(10):1085, 2003. ISSN 1525-2027.

B.A. Brooks, M. Bevis, K. Whipple, J.R. Arrowsmith, J. Foster, T. Zapata, E. Kendrick, E. Minaya, A. Echalar, M. Blanco, et al. Orogenic-wedge deformation and potential for great earthquakes in the central andean backarc. *Nature Geoscience*, 4(6):380–383, 2011.

M. Chlieh, JB De Chabalier, JC Ruegg, R. Armijo, R. Dmowska, J. Campos, and KL Feigl. Crustal deformation and fault slip during the seismic cycle in the North Chile subduction zone, from GPS and InSAR observations. *Geophysical Journal International*, 158(2):695–711, 2004. ISSN 1365-246X.

M. Chlieh, H. Perfettini, H. Tavera, J.P. Avouac, D. Remy, J.M. Nocquet, F. Rolandone, F. Bondoux, G. Gabalda, and S. Bonvalot. Interseismic coupling and seismic potential along the central andes subduction zone. *Journal of Geophysical Research*, 116(B12):B12405, 2011.

E. Contreras-Reyes, E.R. Flueh, and I. Grevemeyer. Tectonic control on sediment accretion and subduction off south central Chile: Implications for coseismic rupture processes of the 1960 and 2010 megathrust earthquakes. *Tectonics*, 29(6), 2010. ISSN 0278-7407.

E. Contreras-Reyes, J. Jara, I. Grevemeyer, S. Ruiz, and D. Carrizo. Abrupt change in the dip of the subducting plate beneath north chile. *Nature Geoscience*, 5(5):342–345, 2012.

Charles DeMets, Richard G Gordon, and Donald F Argus. Geologically current plate motions. *Geophysical Journal International*, 181(1):1–80, 2010.

R. DeMets Gordon. Effect of recent revisions to the geomagnetic reversal rimescale on estimates of current plate motions, Geophys. *Rev. Lett*, 2(20):2191–2194, 1994.

A. Fuenzalida, B. Schurr, M. Lancieri, and RI Madariaga. High-resolution relocation and mechanism of aftershocks of the 2007 tocopilla (chile) earthquake. *in press to Geophysical Journal International*, 2013.

E. Kendrick, M. Bevis, R. Smalley, et al. The Nazca-South America Euler vector and its rate of change. *Journal of South American Earth Sciences*, 16(2):125–131, 2003. ISSN 0895-9811.

J.P. Loveless and B.J. Meade. Spatial correlation of interseismic coupling and coseismic rupture extent of the 2011 mw= 9.0 tohoku-oki earthquake. *Geophys. Res. Lett*, 38:L17306, 2011.

E. Norabuena, L. Leffler-Griffin, A. Mao, T. Dixon, S. Stein, I.S. Sacks, L. Ocola, and M. Ellis. Space geodetic observations of Nazca-South America convergence across the central Andes. *Science*, 279 (5349):358, 1998.

S. Peyrat, R. Madariaga, E. Buforn, J. Campos, G. Asch, and J. P. Vilotte. Kinematic rupture process of the 2007 Tocopilla earthquake and its main aftershocks from teleseismic and strong-motion data. *Geophysical Journal International*, 182(3):1411–1430, September 2010. ISSN 0956540X. doi: 10.1111/j.1365-246X.2010.04685.x. URL `http://doi.wiley.com/10.1111/j.1365-246X.2010.04685.x`.

JC Savage. A dislocation model of strain accumulation and release at a subduction zone. *Journal of Geophysical Research-Solid Earth*, 88(B6), 1983.

C. Vigny, A. Rudloff, J.C. Ruegg, R. Madariaga, J. Campos, and M. Alvarez. Upper plate deformation measured by GPS in the Coquimbo Gap, Chile. *Physics of the Earth and Planetary Interiors*, 175 (1-2):86–95, 2009. ISSN 0031-9201.